

Investigations of the plume accompanying pulsed ultraviolet laser ablation of graphite in vacuum

Frederik Claeysens, Robert J. Lade,^{a)} Keith N. Rosser, and Michael N. R. Ashfold^{b)}
School of Chemistry, University of Bristol, Bristol BS8 ITS, United Kingdom

(Received 17 July 2000; accepted for publication 6 October 2000)

The plume accompanying 193 nm pulsed laser ablation of graphite in vacuum has been studied using wavelength, time and spatially resolved optical emission spectroscopy and by complementary Faraday cup measurements of the positively charged ions. The temporal and spatial extent of the optical emissions are taken as evidence that the emitting species result from electron-ion recombination processes, and subsequent radiative cascade from the high n, l Rydberg states that result. The distribution of C neutral emission is symmetric about the surface normal, while the observed C^+ emission appears localized in the solid angle between the laser propagation axis and the surface normal. However, Faraday cup measurements of the ion yield and velocity distributions, taken as a function of scattering angle and incident pulse energy, indicate that the *total* ion flux distribution is peaked along the surface normal. The derived ion velocity distributions are used as input for a two-dimensional model which explains the observed anisotropy of the C^+ emission in terms of preferential multiphoton excitation and ionization of C species in the leading part of the expanding plasma ball that are exposed to the greatest incident 193 nm photon flux, prior to electron-ion recombination and subsequent radiative decay. © 2001 American Institute of Physics. [DOI: 10.1063/1.1330548]

I. INTRODUCTION

After a lengthy induction period, interest in, and use of, pulsed laser ablation (PLA) as a route to depositing thin films (of, for example, metals, carbon, oxides, and other ceramics, ferroelectrics and high- T_c superconductors) on a wide variety of substrate materials at room temperature, is now growing rapidly.¹ Film formation by pulsed laser deposition (PLD) was first reported in 1965,² but many details of the chemical physics involved in the deposition process are still far from completely understood. The process is often envisaged as a sequence of steps, initiated by the laser radiation interacting with the solid target, absorption of energy and localized heating of the surface, and subsequent material evaporation. The properties and composition of the resulting ablation plume may evolve, both as a result of collisions between particles in the plume and through plume-laser radiation interactions. Finally the plume impinges on the substrate where incident material may be accommodated, rebound back into the gas phase, or induce surface modification (via sputtering, compaction, subimplantation, etc.). Such a separation has conceptual appeal, but is necessarily oversimplistic. Furthermore, the laser-target interactions will be sensitively dependent both on the nature and condition of the target material, and on the laser pulse parameters (wavelength, intensity, fluence, pulse duration, etc.). Subsequent laser-plume interactions will also be dependent on the properties of the laser radiation, while the

evolution and propagation of the plume will also be sensitive to collisions and thus to the quality of the vacuum under which the ablation is conducted and/or the presence of any background gas. Obviously, the ultimate composition and velocity distribution (or distributions, in the case of a multi-component ablation plume) of the ejected material is likely to be reflected in the detailed characteristics of any deposited film.

Here we report studies of the ablation plume accompanying ArF (193 nm) pulsed laser ablation of graphite. Graphite is an attractive target material for fundamental studies of PLA, both because of its intrinsic elemental simplicity and because of the wide potential applicability of hard hydrogen-free diamondlike carbon (DLC) films.³ It has been the subject of several previous investigations; indeed graphite was one of the first target materials to be ablated when the pulsed ruby laser first became available.⁴ Subsequent studies of the PLA of graphite using long excitation wavelengths (e.g., 1064 nm) have shown the ablation plume to contain a high proportion of small carbon cluster species (ions and neutrals).⁵⁻⁷ DLC films in which an estimated 70% of the C atoms show sp^3 (tetrahedral) coordination have been reported following 1064 nm laser ablation of graphite in vacuum, but only at laser intensities approaching 10^{10} W cm⁻².⁸ Such observations should be contrasted with PLA induced using short wavelength ultraviolet (UV) laser radiation (e.g., 193 nm radiation), where the plume is dominated by atomic species (C neutrals and ions),⁹⁻¹¹ and high quality DLC films containing >90% sp^3 bonded C atoms have been reported using much lower intensities ($\sim 5 \times 10^8$ W cm⁻²).^{8,12-15} Such observations support the consensus view that high (~ 100 eV) impact energies encourage formation of dense sp^3 (rather than graphitic) networks in the de-

^{a)}Current address: Kidde International, Mathisen Way, Slough, Berks SL3 0HB, United Kingdom.

^{b)}Author to whom correspondence should be addressed. TEL: +44 117 9288312; Fax: +44 117 9250612; electronic mail: mike.ashfold@bris.ac.uk

posited film,^{3,16–21} and that high ejection velocities are a feature of electronic (i.e., UV) rather than thermally driven material ablation. Nonetheless, many details of the ablation process including, for example, factors which affect the plume composition and properties, and how these in turn influence the resulting film characteristics, merit further study.

The present work focuses on an improved characterization of the plume accompanying PLA of graphite at 193 nm in vacuum, using a combination of wavelength, temporally and spatially resolved optical emission spectroscopy (OES), together with Faraday cup measurements of charged particle production. The temporal and spatial extent of the optical emissions suggest that the emitting species arise as a result of electron–ion recombination, and subsequent radiative cascade from the high Rydberg states that result from this association. The C neutral emission is observed to be distributed symmetrically about the surface normal, but the observed C⁺ emission is localized in the solid angle between the laser propagation axis and the surface normal. Time-of-flight (TOF) and time gated imaging studies of the optical emission can provide measures of the plume expansion characteristics, as can a variety of electrostatic probe measurements. The results of preliminary Langmuir probe measurements of both ions and electrons in the plume accompanying 193 nm ablation of graphite have been reported previously.¹¹ These indicated similar recoil velocities for both species. Here we also report complementary Faraday cup measurements of the ion yield and velocity distributions, as a function of scattering angle, and the dependence of these measurables on the incident pulse energy. These results serve as input for a simple two-dimensional (2D) model which provides a rationale for the observed anisotropy of the C⁺ emission in terms of preferential multiphoton excitation (and ionization) of C atoms in the leading part of the expanding plasma ball that are exposed to the greatest incident 193 nm photon flux.

II. EXPERIMENT

Aspects of the apparatus and experimental procedure have been reported previously.^{11,22} The output of an excimer laser (Lambda-Physik, Compex 201) operating on ArF (193 nm, 10 Hz repetition rate) is steered using two (or three) dichroic mirrors, apertured with an iris and focused (20 cm f.l. lens) so as to be incident on a graphite target located in a stainless steel vacuum chamber maintained at $\sim 10^{-6}$ Torr. Throughout this text laser output energies are quoted. These can be as high as 300 mJ pulse⁻¹ with a fresh gas fill, but the combined effects of the steering mirrors, iris and entrance window ensure that only $\sim 40\%$ of this pulse energy reaches the target. The target design and manipulation has evolved with time,^{11,22} but all experiments reported in this work involved use of one or other of the two following arrangements: Target 1 comprised a side-mounted rotatable graphite disk (Poco Graphite Inc., DFP-3-2 grade), with the laser incident at 45° to the surface normal (x); in the more recent arrangement, Target 2, the graphite disk is mounted on a microprocessor controlled 2D translation stage (PIC based Stamp2) so that the focal spot on its front face is on the

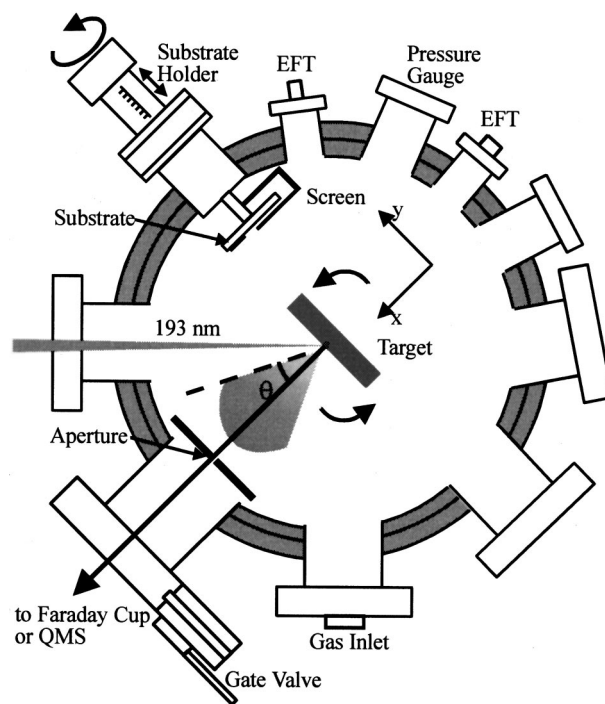


FIG. 1. Plan view of the ablation chamber as configured for the present experiments. The graphite target is shown oriented such that the excimer laser beam is incident at an angle of 45°. θ defines the angle between the surface normal and the detection axis for OES, for example, with positive θ corresponding to angles in the segment between the surface normal and the laser propagation axis. The dashed line indicates the $\theta = +22^\circ$ axis along which maximum C⁺* emission is observed.

center axis of the ablation chamber. Prior to evacuation the entire Target 2 mount can be rotated manually about the vertical axis (z) and locked in any chosen orientation relative to the laser propagation axis. The translation stage rasters the target in the yz plane relative to the fixed laser focus, thereby allowing each laser shot to ablate a fresh area of the graphite surface. The focal spot on the target has a total area $\sim 0.4 \text{ mm} \times 1 \text{ mm}$ (as measured by profilometry), reflecting the rectangular spatial profile of the laser output. Given the 40% transmission to the target, an output pulse energy of 200 mJ concentrated into this spot-size would correspond to an average fluence, $F = 20 \text{ J cm}^{-2}$. The long axis of this profile is normally aligned vertically in the laboratory frame (i.e., along z), but can be rotated through 90° so that the long axis lies in the horizontal (xy) plane by introduction of the third steering mirror. As Fig. 1 illustrates, this chamber is also equipped with a flange designed to support either a Faraday cup detector or a quadrupole mass spectrometer (QMS, Hidden, EQP HAS-SPL-4353), and incorporates a rotatable carousel designed to support up to six 1 cm² substrates. Evacuation, from below, is by means of a 100 mm turbomolecular pump backed by a rotary pump. The chamber is also equipped with appropriate pressure gauges, venting ports, power and electrical feedthroughs (EFTs, e.g., for ion probe measurements), facility for introducing metered gas flows and, in the top flange, a large quartz viewing port.

The focal volume adjacent to the target, and the ablation plume, are both clearly visible via their accompanying optical emission which can be viewed using a quartz fiber bundle

located behind a lens/iris combination and the observation port in the top flange. This arrangement restricts the viewing zone to a vertical column of diameter ~ 2 mm. The other end of the fiber bundle abuts the front slit of either of two monochromators. One is a 125 mm monochromator equipped with a 600 lines/mm ruled grating and a UV extended CCD array detector (Oriol Instaspec IV). This system provides low resolution dispersed emission spectra. The other is a 0.5 m monochromator (Spex 1870) equipped with a 2400 lines/mm holographic grating and the entrance and exit slit widths of which are user selectable. Light emerging from the exit slit of this monochromator is detected with a red sensitive photomultiplier tube (PMT). Higher resolution emission spectra were obtained by scanning the monochromator with the slit widths set narrow and passing the PMT output via a boxcar and a voltage \rightarrow frequency converter to a PC. Alternatively, TOF transients of a given emitting species into the column viewed by the optical fiber were obtained using wider slit widths and fixing the monochromator so as to transmit at the center wavelength of the appropriate emission feature. The PMT output was then directed to a digital oscilloscope (Le Croy 9361) and then, via a GPIB interface, to the PC for storage and subsequent data processing. Zero time was established by monitoring the signal from a fast photodiode positioned so as to detect a fraction of the laser output. Substitution of a CCD camera (Photonic Science) equipped with a time gated ($\Delta t = 100$ ns) image intensifier in place of the lens/fiber bundle assembly and viewing through an appropriate narrow band interference or short-pass cut-off filter, constitutes another time resolved method of monitoring selected emissions. Such images provide a particularly clear visualization of the temporal and spatial evolution of selected emitters within the ablation plume.^{8,11,23,24}

The velocity distributions of the positively charged particles in the ablation plume were also measured by TOF methods, using a Faraday cup detector. This detector consists of a polished stainless steel plate, 15 mm in diameter, mounted 4 mm behind an annulus supported, 85% transmitting, grounded tungsten mesh. The front face of the plate was positioned at a distance $d = 421.7$ mm from the focal spot, along the surface normal (i.e., in the xy plane, at 45° to the laser propagation axis). As Fig. 1 shows, the solid angle subtended by the detector is further restricted by the presence of a 2 mm diam aperture mounted centrally on this axis, in the sidarm supporting the flange that links to the QMS/Faraday cup assembly. The detector was maintained at a potential of -20 V; the current transient associated with the positively charged component in each ablation pulse was recorded using the oscilloscope and PC as for the optical transients, as a function of incident pulse energy, and generally summed over 100 consecutive ablation events.

III. RESULTS AND DISCUSSION

A. Wavelength dispersed emission

The ablation plume arising in the 193 nm ablation of graphite in vacuum is clearly visible to the naked eye. When viewed from above, at lower fluences ($F \sim 25$ J cm $^{-2}$), the plume appears as a small volume of intense white plasma

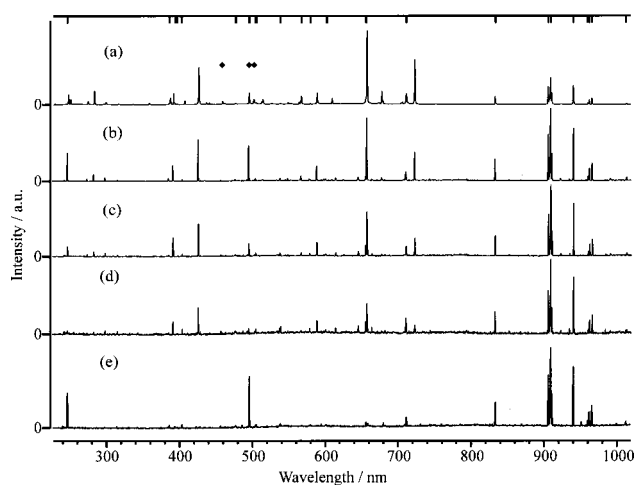


FIG. 2. Wavelength dispersed spectra of the plume emission accompanying 193 nm PLA of graphite in vacuum, using 200 mJ pulse $^{-1}$ incident at 45° to the surface normal and with the long axis of the laser pulse aligned vertically. Spectra (a)–(d) were recorded along the shaft of purple emission, i.e., at $\theta \sim +22^\circ$ to the surface normal, viewing at distances $d = 3, 7, 12,$ and 20 mm from the focal region, respectively. Contrast (b) with the spectrum shown in (e), also taken at $d = 7$ mm, but now monitoring along the $\theta \sim -22^\circ$ axis. C* emission lines are indicated by the comb above (a), ◆ indicates lines appearing in second order, while all other lines are associated with C $^+$ or C $^{2+}$ ions.

localized at the laser focus, and a more extensive diffuse green emission, which appears symmetrically distributed about the surface normal and fills the major part of the forward hemisphere. Occasional thin bright tracks originating from the focal volume with seemingly random trajectories are also evident. These we attribute to incandescent sputtered macroparticles.²² At higher F , these emissions are supplemented by a shaft of purple fluorescence, also originating from the focal volume. This emission appears to be distributed asymmetrically with respect to about the surface normal. Indeed, when the long axis of the rectangular laser output is parallel to the viewing axis (i.e., along z) the purple shaft looks to follow an axis that approximately bisects the laser propagation axis and the surface normal.

Figure 2 shows several low resolution ($\Delta\lambda = 0.8$ nm) wavelength dispersed emission spectra covering the range 225–1025 nm recorded from localized regions of the ablation plume resulting from 193 nm PLA of graphite in vacuum, using a laser output of 200 mJ pulse $^{-1}$ (with its long axis aligned vertically) incident at 45° to the surface normal. Spectra (a)–(d) were recorded along the shaft of purple emission, i.e., at $\theta \sim +22^\circ$ to the surface normal (positive θ corresponds to angles on the same side of the surface normal as the laser propagation axis, as shown in Fig. 1), viewing at distances $d = 3, 7, 12,$ and 20 mm from the focal region. Contrast spectrum (b) with that shown in (e), which was also recorded at $d = 7$ mm but now monitoring along the $\theta \sim -22^\circ$ axis. Each such spectrum was obtained by joining three overlapping 300 nm sections recorded using the Instaspec IV system (30 laser shot accumulations). The displayed spectra have not been corrected for the wavelength dependence of the quartz fibre bundle transmission, the grating reflectivity, or the efficiency of the CCD array detector;

the overall detection sensitivity peaks at ~ 620 nm and is at least four times lower at the two extremes of the range displayed. All features in these spectra can be assigned in terms of monatomic carbon species—neutrals and cations. Indeed, spectrum (a) exhibits *all* of the more intense documented^{25,26} transitions of C and C⁺ that lie in this wavelength range (suggesting a lack of specificity in the excited state production process), while only emissions associated with neutral C atoms are apparent in spectrum (e). Additional lines, e.g., at 501.76 nm, 495.76 nm and 459.45 nm, are transitions appearing in second order associated with, respectively, the C⁺ ($2p^3; ^2D^o \rightarrow 2s^1 2p^2; ^2P$) multiplet at ~ 251.1 nm, the $2p^1 3s^1; ^1P^o \rightarrow 2p^2; ^1S$ transition of atomic C at 247.86 nm, and the $2p^2; ^1D \rightarrow 2s^1 2p^1; ^1P^o$ transition of the C²⁺ dication at 229.69 nm. Comparing such spectra recorded at a range of positions in the plume and at a range of incident fluences reveals that (i) the C²⁺ feature is observed only at small d and at the highest F ; (ii) the C⁺ emission line intensities are greater (relative to those associated with neutral C atoms) at smaller d and at higher F ; and (iii) only neutral C emission lines are detected in regions remote from the focal spot and the purple shaft (e.g., at $d \geq 3$ mm for all $\theta \leq 0^\circ$). Findings (i) and (ii) are in good accord with conclusions reached in a previous OES study of 193 nm laser ablation of graphite,⁹ though we also observe many emission lines at $\lambda > 600$ nm not observed in the earlier work, presumably because of detector insensitivity at these longer wavelengths. In accord with previous studies,^{9,11,27} we see no emission attributable to electronically excited *molecular* species in any of these spectra, though the characteristic Swan band ($d^3\Pi_g \rightarrow a^3\Pi_u$) emission of C₂ is clearly visible when the ablation is carried out in background pressures of < 1 Torr (< 133 Pa) of He or Ar. OES, of course, only provides information about the (generally small) fraction of material that happens to be present in states that decay radiatively. Nonetheless, our preliminary QMS measurements of the energetic positively charged component of the plume generated by 193 nm PLA of graphite in vacuum reinforce the view that the plume is predominantly atomic in composition. Preliminary QMS investigations of the ionic fraction show just three peaks—a dominant peak with mass to charge (m/z) ratio 12 and weak features with m/z 13 and 6, which are most readily attributed to ¹²C⁺, ¹³C⁺, and ¹²C²⁺ ions, respectively.

B. Time resolved imaging of species specific emissions

The time evolution of the various emissions was investigated both by time gated CCD imaging and by using the fiber bundle/monochromator/PMT combination to measure TOF transients of wavelength selected emissions through a spatially localized and defined viewing column. Figures 3(a)–3(c) display time gated ($\Delta t = 100$ ns) intensified CCD images obtained by monitoring all detectable emission transmitted by a long wavelength band pass filter opaque to $\lambda < 780$ nm, recorded at three different times following 193 nm PLA of graphite in vacuum. Again, the long axis of the laser output was aligned vertically in the laboratory frame. 0 mm defines the front face of the graphite target, and the laser pulse is incident at 45° to the surface normal. Analysis of the

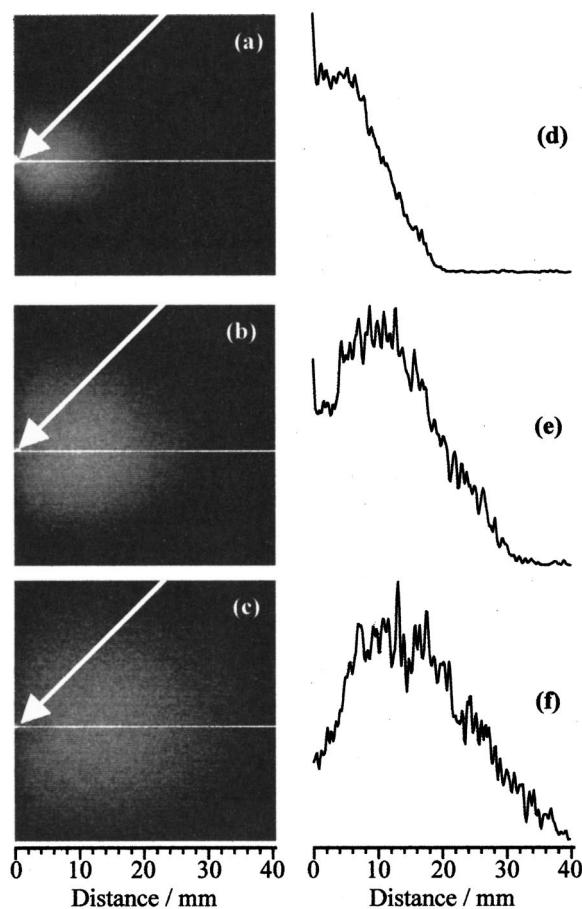


FIG. 3. CCD images of neutral C atom emission with $\lambda > 780$ nm, recorded with the intensifier time gate ($\Delta t = 100$ ns) centered at (a) 430 ns, (b) 630 ns, and (c) 830 ns, following 193 nm PLA of graphite in vacuum. 0 mm defines the front face of the graphite target, the horizontal white line represents the surface normal, and the laser pulse is incident at 45° to the surface normal as indicated by the white arrow, with its long axis aligned along z . (d)–(f) show the corresponding plots of emission intensity versus distance along the surface normal (x).

wavelength dispersed spectra (Fig. 2) reveals that neutral C atoms are the sole carriers of such emission. Obviously, the measured images are “squashed” 2D projections of a 3D cloud of emitting particles. Nonetheless, it is instructive to analyze such images in order to gain some measure of the radial velocity distribution. The right hand panels (d)–(f) show plots of emission intensity versus distance along the surface normal which, in this case, corresponds to the axis of maximum emission intensity. Figure 4 shows a plot showing the x value of the median of the intensity distribution (i.e., the point dividing the faster and slower halves of the distribution) measured in a series of such images taken every $0.1 \mu\text{s}$ after the laser pulse vs delay time; the gradient of the line of best fit implies a mean propagation velocity for the distribution of emitting neutral C atoms, $v_n = 21 \pm 1 \text{ km s}^{-1}$. Image analysis also allows estimation of the full-width half-maximum (FWHM) velocity spreads of the measured emission intensity profiles along any selected slice, e.g., parallel (δv_x) and perpendicular (δv_y) to the propagation axis. Dispersion velocities $\delta v_x = 28 \pm 1 \text{ km s}^{-1}$ and $\delta v_y = 24 \pm 1$

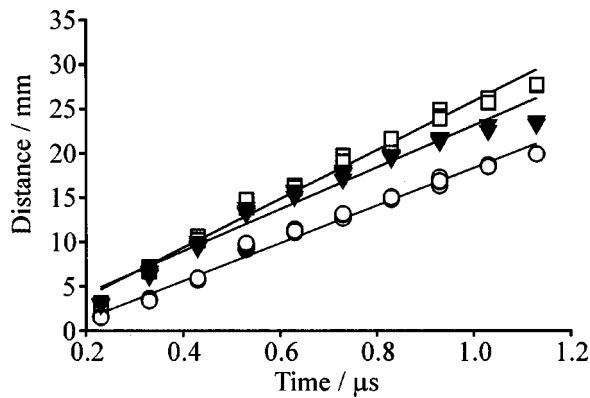


FIG. 4. Medians of the intensity distributions along x (O), and FWHMs (δv_x (\square) and δv_y (\blacktriangledown), derived from time gated CCD images of the neutral C atom emission such as shown in Figs. 3(d)–3(f), recorded as a function of delay time after the laser pulse. The gradients of the lines of best fit give one measure of the propagation and dispersion velocities for the emitting neutral C atoms, $v_n = 21 \pm 1 \text{ km s}^{-1}$, $\delta v_x = 28 \pm 1 \text{ km s}^{-1}$, $\delta v_y = 24 \pm 1 \text{ km s}^{-1}$.

km s^{-1} were derived in this way, suggesting that the emitting C atom component within the ablation plume is propagating and expanding at comparable rates.

Such behavior should be contrasted with that displayed by the emitting C^+ ions, which we choose to monitor via the $4f^1;^2F^o \rightarrow 3d^1;^2D$ transition at $\sim 426.71 \text{ nm}$. This closely spaced doublet emission was isolated by imaging through a narrow band interference filter with peak transmission at 426.7 nm and 3 nm transmission FWHM. As Fig. 5 shows, the C^+ emission following irradiation of the graphite target with the beam incident at 45° to the surface normal is concentrated in a faster moving plasma ball that evolves along an axis roughly midway between the laser propagation axis and the surface normal. As with the neutral C atom emissions discussed above, analysis of such time-gated images provides a measure of the mean propagation velocities of the emitting C^+ ions ($\bar{v}_+ \sim 40 \pm 1 \text{ km s}^{-1}$ along the $\theta = +22^\circ$ axis) and of the dispersion velocities parallel and perpendicular to this axis ($\delta v_{\text{par}} = 11 \pm 1 \text{ km s}^{-1}$ and $\delta v_{\text{perp}} = 16 \pm 1 \text{ km s}^{-1}$, respectively). Figure 6 shows “white” images (i.e., obtained with no filter on the camera) taken at three other angles of incidence (11° , 30° , and 60°). These serve to confirm the generality of the observation that the C^+ emission accompanying 193 nm ablation of graphite in vacuum (with the long axis of the laser output aligned along z) expands along an axis that is approximately centered on the angle bisecting the laser propagation axis and the surface normal. Previous studies^{8,23} of pulsed laser ablation of graphite at both 193 nm and 248 nm have noted the different propagation characteristics of the C^+ and C emission components, but the directionality of the ball of C^+ emission was less evident. Figure 7 suggests a possible explanation. The ball of C^+ emission observed when the laser is incident at $\theta = 45^\circ$, but with the long axis of the output now aligned along y (i.e., rotated so as to be perpendicular to the observation axis), is observed to propagate along $\theta \sim 10^\circ$ (i.e., much closer to the surface normal). Analysis of a time sequence of such images yields a mean propagation velocity, $\bar{v}_+ \sim 40 \pm 1 \text{ km s}^{-1}$ along the $\theta = 10^\circ$ axis, and dispersion

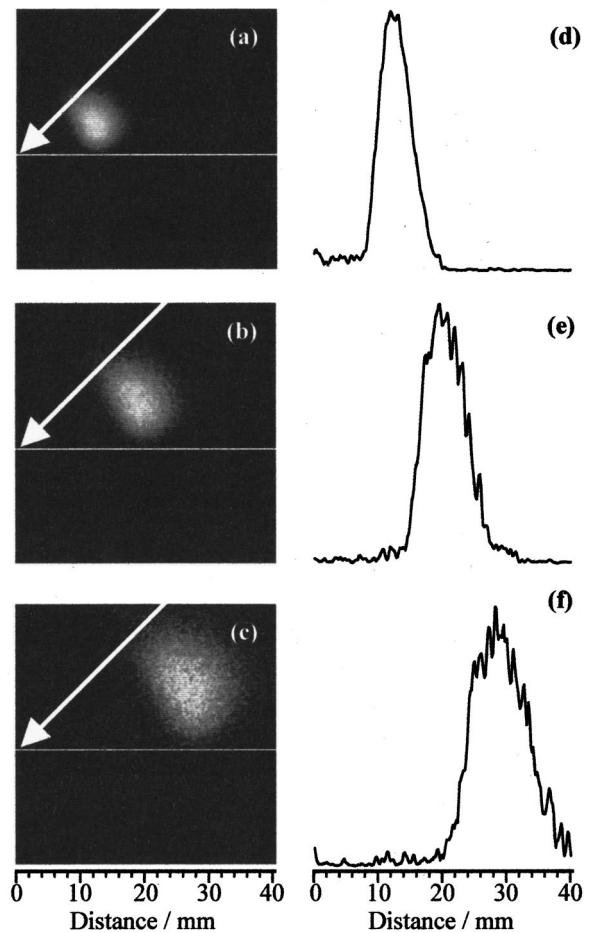


FIG. 5. Time-gated ($\Delta t = 100 \text{ ns}$) intensified CCD images of the 426.71 nm C^+ emission accompanying 193 nm PLA of graphite in vacuum. The three time windows shown are as in Fig. 3 and, as in that figure, 0 mm defines the front face of the graphite target, and the laser pulse is incident at 45° to the surface normal (indicated by the horizontal line) and with its long axis aligned along z . (d)–(f) show the corresponding plots of emission intensity vs distance along the $\theta = +22^\circ$ axis.

velocities parallel and perpendicular to this axis ($\delta v_{\text{par}} = 17 \pm 1 \text{ km s}^{-1}$ and $\delta v_{\text{perp}} = 11 \pm 1 \text{ km s}^{-1}$), very similar to those measured with the laser pulse output aligned along z .

Such species selective, time lapse images of the plume provide one direct, and very visual, means of monitoring the ablation plume and of estimating the propagation velocities of the various constituents within the plume. The fiber bundle and Spex monochromator plus PMT assembly allows measurement of TOF transients of wavelength selected emissions through a user defined, and spatially localized, viewing region. It therefore provides an alternative route to estimating plume expansion properties. Figure 8 displays representative transients recorded for the C^+ ion emission at 426.71 nm with the viewing column centered at, respectively, $d = 4, 8, \text{ and } 12 \text{ mm}$ from the focal point, and $\theta = +22^\circ$. The accompanying plot of d against \bar{t} (the time corresponding to the median of the emission waveform) is linear; its slope implies a propagation velocity $\bar{v}_+ \sim 42 \pm 1 \text{ km s}^{-1}$ for these C^+ ions, in good agreement with that deduced from the time gated imaging above and the value (39 km s^{-1}) estimated by Puretzy *et al.*²³ from analysis of time gated images of the

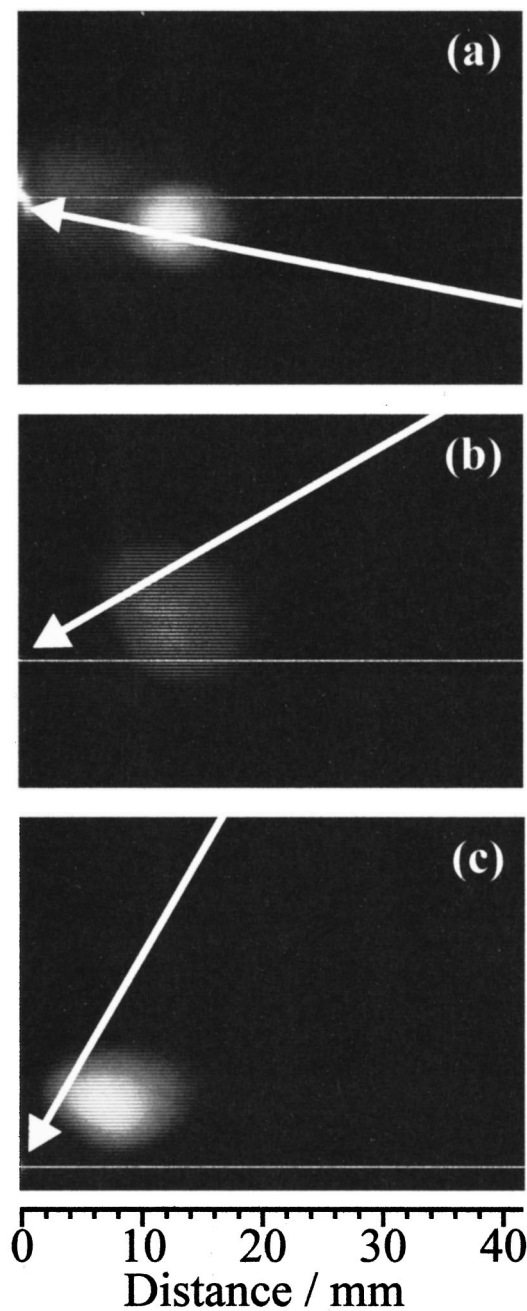


FIG. 6. Time-gated intensified CCD images ($\Delta t = 100$ ns centered at a delay of 430 ns) of the total emission (which, given the camera response function, is dominated by the 426.71 nm transition of C^+) accompanying 193 nm PLA of graphite in vacuum, recorded at (a) 11° , (b) 30° , and (c) 60° . As in Fig. 3, 0 mm defines the front face of the graphite target, the horizontal line indicates the surface normal, and the long axis of the laser output is along z . Each image has been cropped top and bottom for compactness of display.

fastest component in the total emission resulting from ArF laser ablation of graphite in vacuum. C^{2+} cation and C neutral emission features were investigated similarly. TOF spectra of the second order C^{2+} emission, albeit over a much smaller range of d , suggest a similar propagation velocity for these dications directed along $\theta = +22^\circ$, while analyses of TOF transients of selected neutral C emissions (e.g., the intense $^1P^o \rightarrow ^1S$ transition at 247.86 nm) imply $\bar{v}_n \sim 33 \pm 1$ km s $^{-1}$ along the surface normal—somewhat greater than

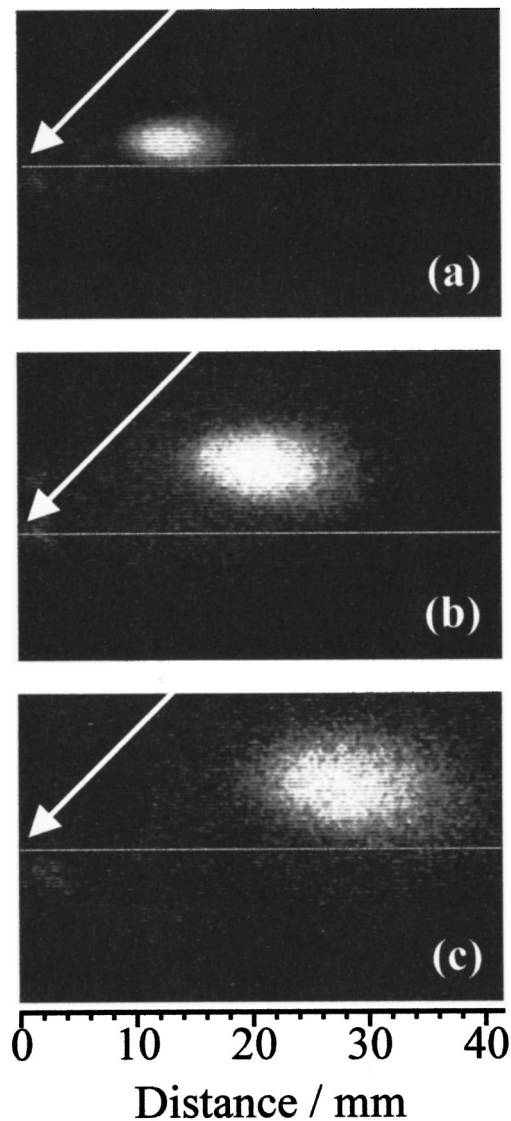


FIG. 7. CCD images of the 426.71 nm C^+ emission, recorded with the intensifier time gate ($\Delta t = 100$ ns) centered at (a) 430 ns, (b) 630 ns, and (c) 830 ns, following 193 nm PLA of graphite in vacuum with the laser pulse incident at 45° to the surface normal. Again, the various images have been cropped top and bottom for display purposes and 0 mm defines the front face of the graphite target but, in contrast to Fig. 5, the long axis of the laser output is now aligned along y (i.e., perpendicular to the observation axis).

that deduced from time gated imaging studies shown in Fig. 3 but still slower than the more localized C^+ ion emission. Before discussing the significance, and some of the limitations of such OES studies, we first consider another type of measurement which can provide complementary information about the motion of positively charged particles in the expanding plume.

C. Faraday cup measurements

Figure 9(a) displays TOF transients of the positively charged material within the ablation plume, obtained using laser output pulse energies of 50, 100, 150, and 200 mJ, each incident at 45° to the surface normal, measured using the Faraday cup detector located on the x axis with its front face at a distance $d = 421.7$ mm from the target. The solid curve

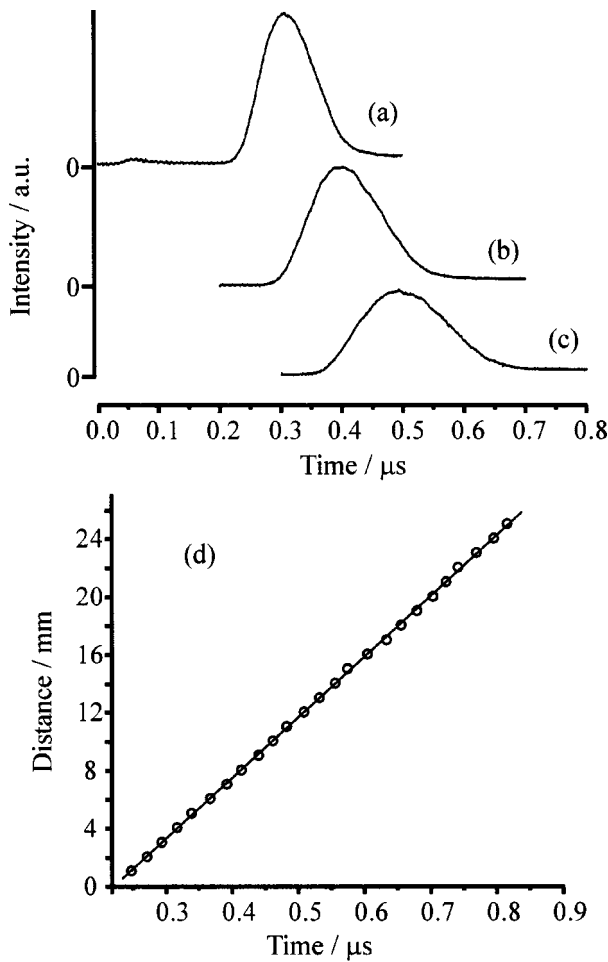


FIG. 8. TOF transients of the C^+ ion emission at 426.71 nm emanating from vertical columns centered at $\theta = +22^\circ$ and at, respectively, $d =$ (a) 4, (b) 8, and (c) 12 mm from the focal origin. The plot (d) of d vs \bar{t} (the time corresponding to the center of gravity of the emission waveform) is linear; its slope implies a propagation velocity $\bar{v}_+ = 42 \pm 1 \text{ km s}^{-1}$.

through the TOF profile recorded at 150 mJ pulse⁻¹ serves to illustrate that the TOF signals $S(x, t)$ are each well described by a shifted Maxwell-Boltzmann velocity distribution of the form,

$$S(x, t) \propto t^{-5} \exp\left\{-\frac{m}{2kT} \left(\frac{x}{t} - u\right)^2\right\}, \quad (1)$$

where $S(x, t)$ is the space- and time-dependent particle flux incident on the Faraday cup detector and t is the TOF, and T (the local equilibrium temperature) and u (the flow velocity parallel to the surface normal) are parameters to be floated in the fit. Such a function is generally assumed to provide a valid description of the TOF profile of ablated flux in cases where a Knudsen layer is formed.^{21,28,29} Given previous estimates¹¹ (from target mass loss measurements) that the C atom removal rate in these experiments is $\sim 10^{15} \text{ pulse}^{-1}$ when using an output energy of 200 mJ pulse⁻¹, together with representative collision cross section and velocity values of $\sim 0.2 \text{ nm}^2$ and 40 km s^{-1} , respectively, the requisite few collisions deemed necessary for Knudsen layer formation close to the surface will occur within the first few ns of the laser pulse. We note, in passing, that there is some am-

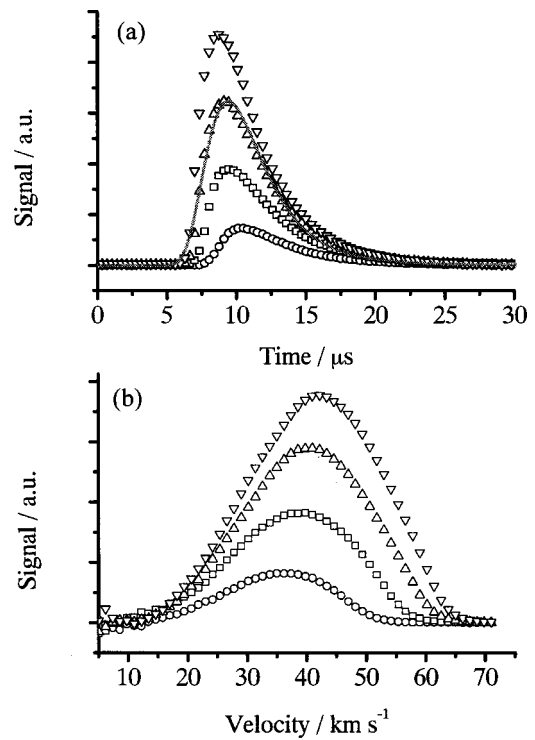


FIG. 9. (a) TOF transients of the positively charged component of the ablation plume resulting from 193 nm PLA of graphite in vacuum, using output pulse energies of 50 (O), 100 (\square), 150 (\triangle), and 200 mJ (∇) each incident at 45° to the surface normal, measured using the Faraday cup detector positioned at a distance $d = 421.7 \text{ mm}$ from the target. The solid curve through the 150 mJ profile shows the result of a least squares fit in terms of Eq. (1), with best-fit parameters $u = 30.5 \text{ km s}^{-1}$ and $T = 185\,000 \text{ K}$. (b) shows the velocity distributions that derive from the experimental TOF profiles.

biguity in the literature as to whether the appropriate pre-exponential factor in Eq. (1) when using a flux-sensitive detector should include a t^{-5} or t^{-4} term. In practice, either function gives an equally good fit to TOF profiles such as those shown in Fig. 9; the best-fit T values are found to decrease and the best-fit u values to increase, in both cases by $< 10\%$, if the pre-exponential term in eq. (1) involves t^{-4} rather than t^{-5} .

The velocity distributions that derive from these TOF profiles, displayed in Fig. 9(b), show that both the total ion signal and the median, v_+ , of each velocity distribution scale with increasing incident energy. These trends are summarized in Fig. 10, where the mean ion kinetic energy has been calculated on the assumption that the charged particles have m/z 12. Interestingly, the plot of kinetic energy vs incident pulse energy [Fig. 9(c)], though roughly linear, has a much shallower slope than that reported previously in the case of 308 nm ablation of graphite in vacuum.²¹ Figure 9(a) reveals ion production at very low incident fluences, in marked contrast to the OES measurements in which formation of *electronically excited* C^+ ions (i.e., the purple shaft) was evident only above a certain threshold energy, but the deduced velocities (e.g. $v_+ = 42.5 \pm 1 \text{ km s}^{-1}$ for an output pulse energy of 200 mJ) match well with those derived from the OES studies of C^+ emission. However, the CCD imaging studies also showed the distribution of emitting C^+ species

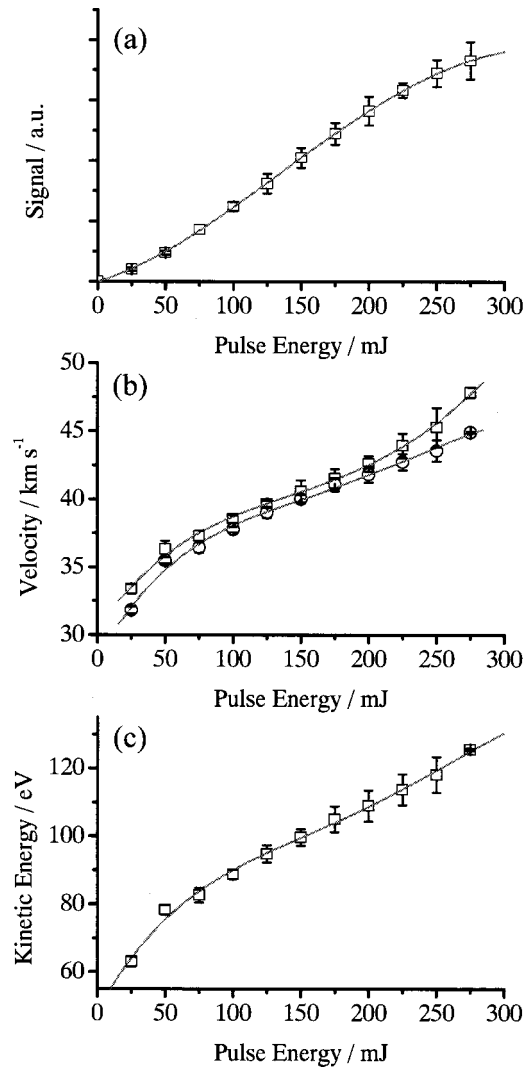


FIG. 10. Plots illustrating the variation of (a) total ion yield, (b) the most probable velocity, v_{mp} (\square), and the median velocity, v_+ (\circ), and (c) the mean ion kinetic energy (calculated on the assumption that the charged particles have m/z 12) with pulse energy, using 193 nm pulses, incident at 45° to the surface normal, on a graphite target in vacuum. The error bars in (a) show the reproducibility of five separate measurements of relative signal strengths as a function of pulse energy, each set of which has been arbitrarily normalized to the unit signal at $E=75$ mJ pulse $^{-1}$, while those in (b) and (c) are standard deviations (1σ) of the absolute velocities determined from, typically, five measurements at each energy. The solid curves in each plot are fourth order polynomial fits to the various data sets.

to be highly asymmetric about the surface normal—at variance with previous ion probe studies which suggested a far more uniform recoil distribution of the *total* ion flux.¹¹

This paradox has been investigated further using the Faraday cup assembly. Experimental constraints mean that the axis along which the laser is incident and the ion detection axis had to be held constant. To investigate the variation in scattered ion flux with θ (i.e., relative to the surface normal), it was thus necessary to vary the angle of incidence on the target, by rotating the target assembly about the z axis, and measuring TOF transients such as those shown in Fig. 9, as a function of both the laser pulse energy and its angle of incidence. Inevitably, this procedure must cause some change in the footprint of the focal spot on the target, and thus in the

incident fluence at any given pulse energy. Nonetheless, as Fig. 11(a) shows, the angular distribution of the total ion flux measured in this way, at all incident fluences, peaks at $\theta = 0^\circ$ (in contrast to the OES observations) and conforms to a $\cos^q\theta$ distribution with $q \sim 5$, thereby reinforcing previous conclusions²² that the distribution of the total ion flux distribution is considerably more isotropic than that of the C^+ ions evident in OES. Given this grid of measured TOF spectra it is also possible to determine the way the velocity distribution varies with scattering angle. Knowing d , it is possible to transform any measured TOF profile into the associated velocity distribution; Fig. 11(b) shows that the median velocity, v_+ , also peaks at $\theta \sim 0^\circ$ and exhibits an angular dependence that scales as $\cos^q\theta$, with a best-fit q value that rises from ~ 0.8 (for 50 mJ output pulses) to ~ 1.3 (when using 200 mJ pulses). It is also possible to fit each measured TOF profile in terms of a function analogous to Eq. (1) but which now, since we are concerned with material ejection along axes other than the surface normal, involves velocity components both parallel and perpendicular (y) to x , i.e.,

$$S(x_i, y_i, t) \propto A t^{-5} \exp \left\{ -\frac{m}{2kT_x} \left(\frac{x_i}{t} - u \right)^2 - \frac{m}{2kT_y} \left(\frac{y_i}{t} \right)^2 \right\}. \quad (2)$$

Only T_y was floated when fitting TOF spectra recorded at $\theta \neq 0^\circ$; u and T_x were clamped at the values determined from analysis of TOF spectra of ions ejected along the surface normal [i.e., using Eq. (1)] at the same incident pulse energy. Best-fit values of u , T_x , and T_y , and their variation with incident pulse energy, are shown in Figs. 11(c) and 11(d). The corresponding full width half maximum (FWHM) velocity spreads parallel and perpendicular to the surface normal, δv_x and δv_y , are deduced from the relationship

$$\delta v_{x(y)} = \sqrt{\frac{8kT_{x(y)} \ln 2}{m}}, \quad (3)$$

which follows from assuming that the velocity spreads in the x and y directions may be described by Gaussian functions. Reviewing these fits, and the plots shown in Figs. 10 and 11, we note for future reference that the *total* ion distribution in the plume at the highest incident fluences used here is well described by a shifted Maxwell–Boltzmann distribution propagating along the surface normal with a flow velocity, $u \sim 35$ km s $^{-1}$, and dispersion both parallel (δv_x) and perpendicular (δv_y) to this axis of ~ 25 km s $^{-1}$ (FWHM). These values will be used later in a simple model designed to account for the observed asymmetric C^+ emission.

IV. DISCUSSION

Three different strategies, two based on OES, the other on use of a Faraday cup, return similar values for the propagation velocity of the ionic component within the plume arising in the pulsed 193 nm laser ablation of graphite in vacuum. Estimates of the propagation velocity of the neutral atomic C component determined by the two forms of OES

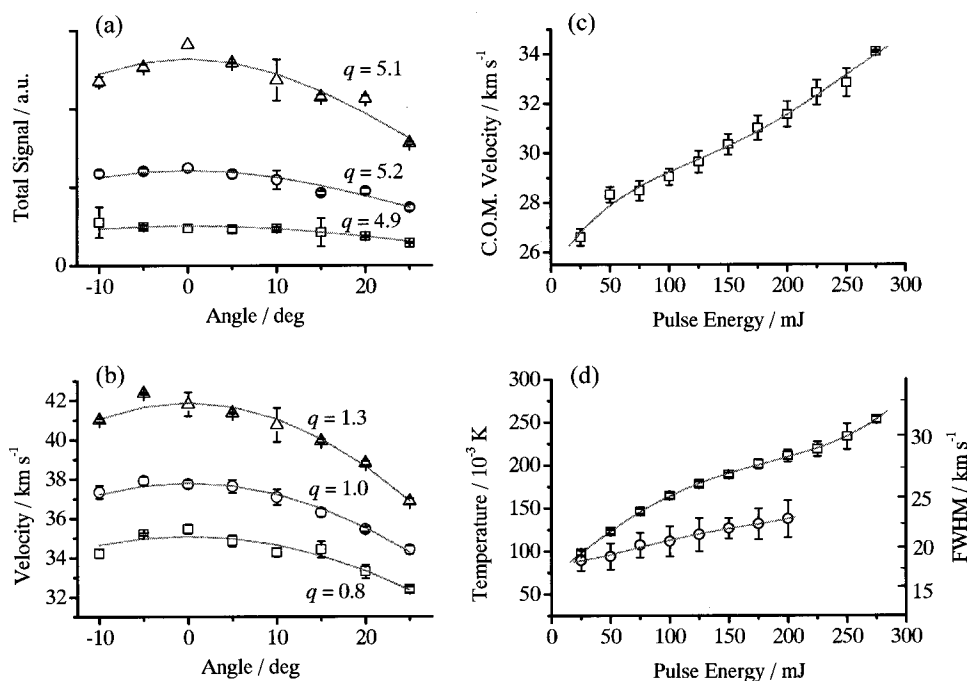


FIG. 11. Plots showing (a) the angular variation of the total positive ion signal arising in the 193 nm PLA of graphite in vacuum, using output pulse energies of 50 (\square), 100 (\circ), and 200 mJ (Δ). These measurements were made by rotating the target so as to vary the angle at which the laser pulse was incident, with the Faraday cup detector fixed on an axis at 45° to the laser propagation axis; (b) the angular variation of the corresponding v_+ values. In both cases, $\theta = 0^\circ$ corresponds to the case that the target surface normal coincides with the detection axis. The smooth curves through the points are fits in terms of $\cos^q \theta$ distributions, with the best fit q value indicated in each case; (c) and (d) show, respectively, the deduced center-of-mass velocity, u , and the velocity dispersion parallel, δv_x (\square), and perpendicular, δv_y (\circ), to the surface normal, each as a function of incident pulse energy. The solid lines in these two panels are fits (using fourth order polynomials) to the data. As in Fig. 9, the error bars in (a) show the reproducibility of several different measurements of relative signal strengths as a function of pulse energy, each set of which has been arbitrarily normalized to be the same signal at $\theta = 0^\circ$, while those in (b), (c), and (d) are standard deviations (1σ) of the absolute velocity spreads determined from the various measurements at each energy.

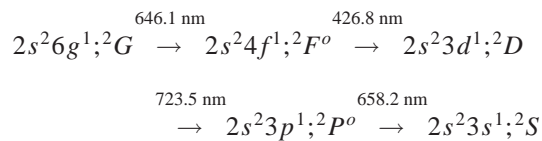
show more variation, but consistently indicate that $\bar{v}_+ > \bar{v}_n$, in accord with previous studies.^{8,10,23} Such observations are consistent with contemporary models of UV laser ablation in which the laser pulse induces localized surface excitation and rapid heating, leading to photo- and thermionic electron emission closely followed by ejection of positive ions, which are accelerated out of the focal volume as a result of Coulombic attraction (by the expanding electron cloud) and repulsion (by other ions at smaller d) before reaching some terminal propagation velocity.³⁰ Species ejected into the vacuum as neutrals are not subject to this Coulombic acceleration, whilst neutrals that result from gas phase ion–electron recombination in the denser (early time) regions of the plume will only experience this acceleration prior to neutralization and thus attain a lower terminal velocity. More careful inspection, however, reveals other differences between the various measurements. Most notably, the CCD imaging studies suggest a far more localized distribution of C^+ species (both in the radial and angular coordinates) than is indicated by either the present, or previous,¹¹ ion probe measurements.

Here we concentrate attention on possible mechanisms for producing the electronically excited species monitored via OES and, in particular, the origin of the localized shaft of C^+ emission. The radiative lifetimes of the various excited species are far shorter than the timescales over which emission is observed. Thus the emission observed at larger d must be from excited states that are populated post-ablation, in the

gas phase, well after cessation of the pulsed laser excitation. Electron impact excitation (EIE) during plume expansion is one possible route for forming excited state species, the efficiency of which should fall with decreasing number density, and thus increasing d . On this basis, EIE induced emission should be most efficient at small d , and thus favor the slower moving particles. That being the case, OES might be expected to underestimate the actual plume propagation velocity. However, the EIE mechanism also requires the electrons and the atoms/ions to be proximate. Given that the electrons and the ions have similar propagation velocities,¹¹ both of which are greater than \bar{v}_n , it might follow that EIE would actually favor that subset of the total flux distribution that was propagating at similar speeds to the expanding electron cloud (i.e., the faster part of the neutral velocity distribution). EIE of C atoms and C^+ ions is generally spin conserving.³¹ Thus, if EIE is the major route to the observed emissions, the fact that *all* C and C^+ emissions that fall within the monitored wavelength range are indeed observed (Fig. 1) would imply the formation of both ground (triplet) and excited (singlet) C atoms in the ablation process. However, many of the emissions originate from very energetic excited states, e.g., the $^4P^0$ excited state of C^+ responsible for the 432.2 nm and 359.1 nm emissions observed along the $\theta = +22^\circ$ axis at short d lies 25.98 eV above the ground state ion and 37.25 eV above the ground state of neutral carbon. Such high levels of excitation are hard to reconcile with simple EIE induced by electrons propagating with mean kinetic energies in

the meV range.¹¹ Neither does an EIE mechanism provide a particularly obvious explanation for the observed highly localized C^+ emission.

Another mechanism for forming electronically excited species is electron-ion recombination (EIR). This requires the presence of a third body to stabilize the recombination product, and should thus also be most important at small d . EIR would encourage the conversion $C^{2+} \rightarrow C^+ \rightarrow C$, in accord with the d dependence of these various species revealed by the OES studies. EIR will favor formation of Rydberg states with high principal quantum number, n , since these recombination products require least energy transfer to the third body. Many of these Rydberg states will be formed not just with high n but also high l (where l is the orbital angular momentum quantum number). Given the $\Delta l = \pm 1$ selection rule associated with allowed radiative transitions, these species can only radiate by a cascade mechanism. The initial steps in this cascade will involve Rydberg-Rydberg transitions at long wavelength; the spatial and temporal extent of the observed emission plumes would then reflect the time taken for the population in high n, l states to cascade down into the observed emitting levels. The observation of emissions from excited states of both C and C^+ involving $\dots ng^1$ and $\dots nf^1$ configurations and of sequences like



in C^+ , encourage the view that radiative cascade accounts for the apparently delayed emission. Clearly, wavelength resolved OES measurements at longer infrared wavelengths would help in confirming the importance of EIR processes.

We now proceed to show how the localized C^+ emission, its directionality, and its sensitivity to the orientation of the laser output, are all explicable in terms of EIR following laser-plasma (rather than laser-target) interactions; indeed, we will show that such observations are a signature of laser-plasma interactions. To this end, we have implemented an approximate 2D ‘‘particle in the cell’’ type model which provides a rationale for the observed anisotropy of the C^+ emissions, and identifies various parameters which will tend to enhance or degrade such anisotropic optical emission from ablation plumes. Key features of the model are summarized in Fig. 12. As in the experiment, the front face of the target lies in the yz plane, with the surface normal directed along x . All of the present calculations consider material ejection just in the xy plane. This space is partitioned into a mesh of 75×75 rectangular grid cells, chosen so as to span the entire ‘‘volume’’ into which sputtered material may have travelled by the cessation of the laser pulse. The pulse of laser radiation (of duration, $\Delta t = 20$ ns) is assumed to have a ‘‘top hat’’ intensity distribution, in both space and time, and to be incident as a parallel shaft in the xy plane, at an angle ϕ to the surface normal, so as to irradiate the target surface over a length distributed symmetrically about the point $y = 0$. This length is treated as 21 identical pixels of width δy , each of which serves as a source of ablated particles. All particles are

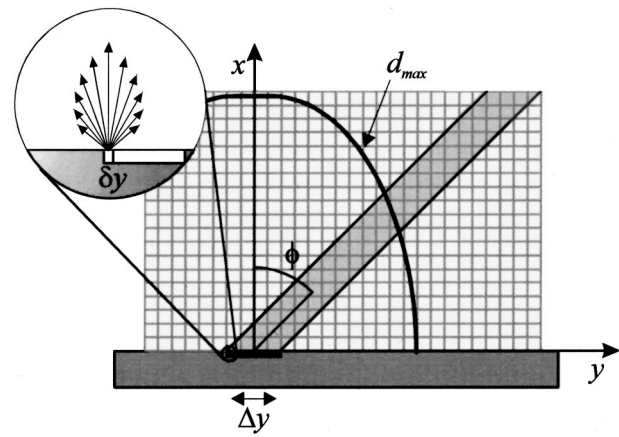


FIG. 12. Illustration of the 2D model to account for the observation of asymmetric C^+ emission. The front face of the target lies in the yz plane, with the surface normal directed along x . The incident laser radiation, and the ejected material, are confined to the xy plane. This space is partitioned into a mesh of 75×75 rectangular grid cells, chosen so as to span the entire xy space into which sputtered material can travel by the cessation of the laser pulse. The pulse of laser radiation (of duration, $t = 20$ ns) is assumed to have a ‘‘top hat’’ intensity distribution, in both space and time, and to be incident as a parallel shaft in the xy plane, at an angle ϕ to the surface normal, so as to irradiate the target surface over a length distributed symmetrically about the point $y = 0$. This length is treated as 21 identical pixels of width δy , each of which will serve as a source of ablated particles, while the ejected particle density from each pixel is distributed over 185 radial spokes, distributed uniformly throughout the angular range $-90^\circ < \theta < 90^\circ$ with a velocity distribution given by Eq. (2).

treated as being identical, and each pixel within the length Δy is assumed to contribute equally to the total ablation yield. In this simple model the ejected particle density from each pixel is distributed over 185 radial spokes, distributed uniformly throughout the angular range $-90^\circ < \theta < 90^\circ$.

Modeling of the laser interaction is subdivided into 20 time steps, each with $\delta t = 1$ ns, so as to span the entire laser pulse duration. During the first time step, δt_1 , a total of N_1 particles are ejected into the gas phase. Each source pixel contributes equally to N_1 . Each ejected particle is given a particular velocity (defined relative to its particular cell origin) chosen such that the ensemble of velocity vectors mimics that deduced from analysis of the ion yield arising in the high fluence regime [i.e., $u = 35 \text{ km s}^{-1}$, and with a Gaussian spread $\delta v_x = \delta v_y = 25 \text{ km s}^{-1}$ (FWHM) in both the x and y directions]. Each particle is ascribed an associated density, ρ_i , which is initially set to unity. This is necessary if, as here, the interest is in possible laser-plume interactions, since plume material in the column exposed to laser irradiation can attenuate the incident beam, and thus reduce the light intensity incident on the target and the ablation yield.^{32,33} This attenuation is modeled using the Beer-Lambert expression,

$$I(d) = I_0 \exp[-\alpha \rho(d)(d_{\max} - d)], \quad (4)$$

where the absorption coefficient, α , is assumed to be intensity independent, $\rho = \sum_i \rho_i$ is the local density within a grid cell distant d from the focal region, and $d_{\max} = (u \cos \phi + 2\delta v_x)\Delta t$ is taken as the maximum distance any material can

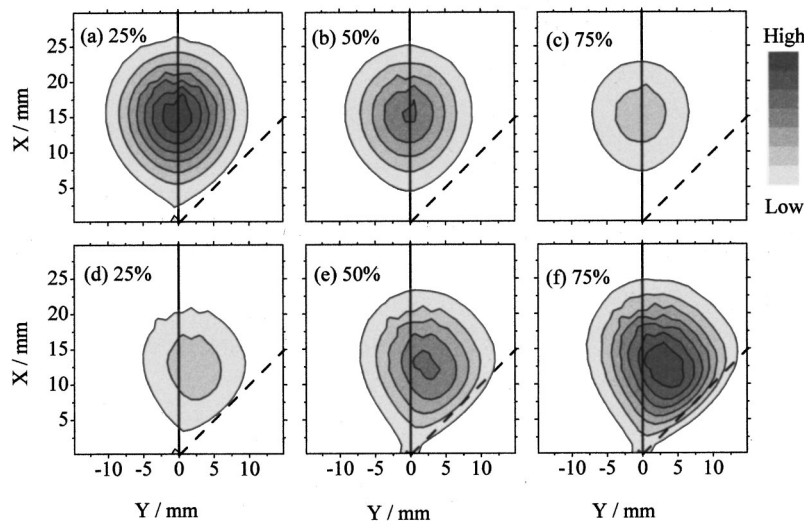


FIG. 13. Linear gray scale plots illustrating the calculated spatial distribution of *total* ablated flux in the *xy* plane at $t=0.5 \mu\text{s}$, for a laser pulse incident at 45° to the surface normal (---), with $\Delta y=0.2 \text{ mm}$ and $\Delta t=20 \text{ ns}$, assuming $u=35 \text{ km s}^{-1}$, $\delta v_x = \delta v_y = 25 \text{ km s}^{-1}$ (FWHM) and three different “strengths” of the absorption coefficient, α [such that the time integrated absorption corresponds to (a) 25%, (b) 50%, and (c) 75% of the incident light intensity, respectively]. Panels (d)–(f) show the calculated distribution of excitation density, ρ , within the plume given these same three absorption strengths. Note that the gray scales used in plots (a)–(c) and (d)–(f) are separately normalized.

propagate within the 20 ns laser pulse duration. In the limit that $\alpha \rightarrow 0$, the incident beam suffers no attenuation and $I(d_{\text{max}}) \equiv I_0$.

During successive time steps, particles generated during all previous time steps will continue to propagate forward, and additional plume material will be produced as a result of the (attenuated) laser beam striking the target surface. To allow for possible plume absorption, the density ρ in each grid cell is calculated at the end of each time step. Equation (3) is then used to calculate the intensity $I(d)$ incident on, and exiting from, each grid cell during the next time step. Consider two neighboring cells along a radius within the irradiated column at positions d_n and d_{n-1} ($d_n > d_{n-1}$), containing respective densities ρ_n and ρ_{n-1} . We define an excitation density $E_n(t)$ for the former grid cell as

$$E_n(t) = \{\rho_n [I(d_n) - I(d_{n-1})]\}(t), \quad (5)$$

for the time step of interest and obtain a final, total excitation density for this cell via the summation $\sum_{t=0}^{20 \text{ ns}} E_n(t)$. Excitation decay is not included in the model. After 20 ns all gas phase material production and excitation is assumed to cease, and the motion of all particles can be extrapolated to longer time to compare with the experimental observations.

Figure 13 shows—in the form of linear gray scale plots—the spatial distribution of *total* ablated flux in the *xy* plane predicted by this model at $t=0.5 \mu\text{s}$, for a beam incident at 45° to the surface normal, with $\Delta y=0.2 \text{ mm}$ and $\Delta t=20 \text{ ns}$, assuming $u=35 \text{ km s}^{-1}$, $\delta v_x = \delta v_y = 25 \text{ km s}^{-1}$ (FWHM) and three different “strengths” of the absorption coefficient, α [such that the time integrated absorption corresponds to (a) 25%, (b) 50%, and (c) 75% of the incident light intensity, respectively]. Clearly, plume absorption reduces the overall ablation yield, but its effect is more obvious in the complementary plots [Figs. 13(d)–13(f)] showing the predicted distribution of excitation density within the plume. The anisotropy evident in these latter plots is reminiscent of that observed in the time gated CCD images of the C^+ emission. Figure 14 shows the predicted variation in the anisotropy of the excitation density with the angle of incidence, ϕ , of the exciting light pulse [(a), top panel], the focal

spot size, Δy [(b), center panel] and the pulse duration [(c), bottom panel]. The qualitative trends evident in (a) and (b) are in accord with the experimental observations (Figs. 6 and 7).

The model calculations support the view that asymmetric plume excitation will generally be most evident in experiments which (as here) involve laser pulses incident at an angle away from the surface normal, of long time duration, and that are tightly focused such that the focal spot size on the target in the viewing plane (Δy) is small compared to the distance (d_{max}) that material can travel during the laser pulse. The simulations shown in Fig. 14 indicate that the anisotropy will be reduced by expanding the size of the focal spot (as found experimentally, Fig. 7), or by reducing the pulse duration. A more critical comparison between experimental observation and the model predictions indicates that the latter tend to underestimate the observed asymmetry of the C^+ emission. Clearly, one contributor to this discrepancy is our use in the model of the “asymptotic” particle velocity distribution, i.e., the distribution measured at long time, after formation of the Knudsen layer. Within the context of the model as posed, however, excitation of gas phase material will be most efficient in the very early part of the laser pulse, before the Knudsen layer is fully developed. Equation (2) with $u \sim 0$ should provide a better description of the initial velocity distribution of the ablated material in the early time, low-density, near collision-free limit. The distribution of excitation density that results from assuming such a function is much more asymmetric. Clearly, a better match with observation can be obtained by making u a time dependent function, but we are satisfied that the present limited calculation suffices to demonstrate the source of the observed asymmetry of the C^+ emission.

Figure 13 also serves to emphasize that such effects will be most evident where there is significant absorption by the plume. Experiments employing longer duration, high energy pulses will tend to produce a longer, denser column of ablated material through which the beam must propagate to reach the target; plume absorption is likely to be more im-

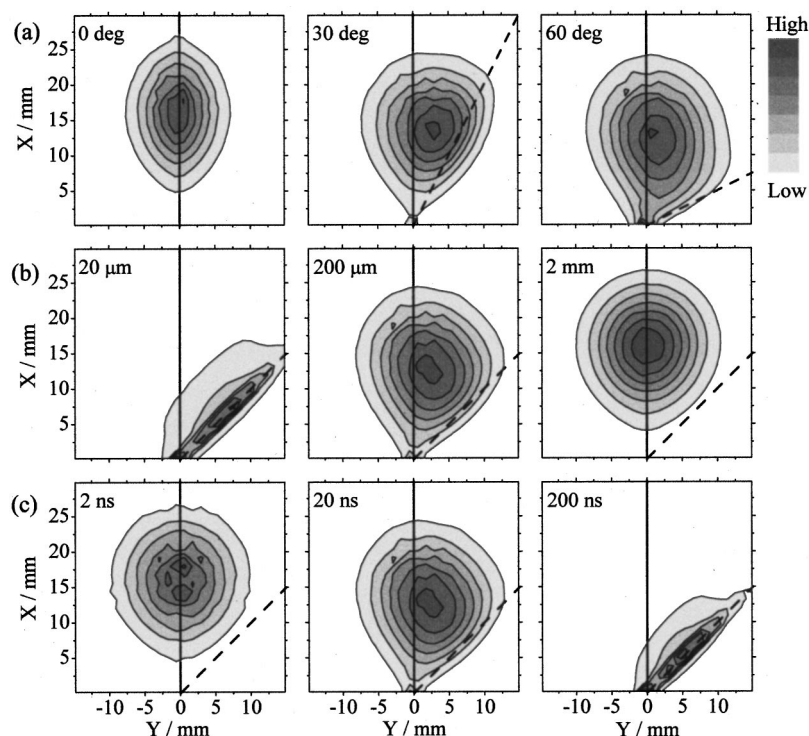


FIG. 14. Predicted variation in the anisotropy of the excitation density, ρ , with (a), (top panel) the angle of incidence, ϕ , of the exciting light pulse (indicated by --), (b), (center panel) the focal spot size, Δy , and (c) (bottom panel) the pulse duration, Δt . Parameters used in the simulations are 200 mJ output pulse energy, $u=35 \text{ km s}^{-1}$, $\delta v_x = \delta v_y = 25 \text{ km s}^{-1}$ (FWHM), 50% absorption by the plume, viewed at $t=0.5 \mu\text{s}$.

portant. Processes that might contribute to the attenuation of incident radiation by an ablation plume include scattering, and absorption—either resonant, or as a result of electron–neutral and/or electron–ion inverse Brehmstrahlung.³⁴ The latter two processes are often discounted as significant contributors to plume absorption when using excimer laser pulses because of the (a) small absorption coefficient of electrons at short excitation wavelengths and (b) presumed low degree of ionization (and thus the electron density). However, this assumption may merit closer scrutiny in the case of both ArF and KrF laser ablation of carbon targets since two low lying metastable excited states of atomic carbon (the $2p^2;^1D$ and $2p^2;^1S$ states) coincidentally have strong one photon absorptions that fall within the respective excimer laser bandwidths.^{25,26} Pappas *et al.*¹² have highlighted the particularly good resonance between the $2p^13s^1;^1P^o \leftarrow 2p^2;^1D$ transition at 193.09 nm and the peak of the ArF excimer laser output. Given that the 1D state of atomic carbon lies at an energy 1.263 eV above that of the 3P ground state, and assuming a typical surface vaporization temperature $T_s \sim 4500 \text{ K}$ in the focal spot on the graphite target, simple thermodynamic considerations would suggest that $\sim 2\%$ of the ablated C atoms will be formed in the metastable excited state. The $2p^13s^1;^1P^o \leftarrow 2p^2;^1D$ transition must provide strong resonance enhancement to the two photon ionization of these atoms in the plume; at the prevailing laser intensities this will be a very efficient process and greatly enhance the local electron and ion densities. This, in turn, will lead to an increase in the local absorption due to electron–neutral and, particularly, electron–ion inverse Brehmstrahlung which, having a continuum spectrum, can interact with *all* photons within the ArF laser bandwidth. Thus the initial resonance enhanced two photon ionization is considered to act as a localized, and highly nonlinear, “seed”

for further absorption and ionization processes, specifically in those regions of the plume that are exposed to the most prolonged and intense laser excitation. These would be the regions identified as receiving the greatest excitation density in the simple model calculations reported above and, qualitatively at least, these correlate with the observed localized shaft of C^+ emission.

V. CONCLUSIONS

Electronically excited species (C atoms, and C^+ and C^{2+} ions) in the plume accompanying 193 nm PLA of graphite in vacuum have been investigated by wavelength, time and spatially resolved OES, while the positively charged component has also been investigated using a Faraday cup detector. The temporal and spatial extent of the optical emissions are explicable if it is assumed that the emitting species result from electron–ion recombination processes, and subsequent radiative cascade from the initially formed high n, l Rydberg states. The C neutral emission is observed to be distributed symmetrically about the surface normal, but the observed C^+ emission is seen to be localized in a rather narrow solid angle between the laser propagation axis and the surface normal. However, the complementary Faraday cup measurements of the ion yield and velocity distributions, as a function of scattering angle and incident pulse energy, indicate that the *total* distribution of positive ions also peaks along the surface normal. The velocity distributions so derived are used as input for a simple two-dimensional model which provides a rationale for the observed anisotropy of the C^+ emission in terms of preferential multiphoton excitation and ionization of C species in the leading part of the expanding plasma ball that are

exposed to the greatest incident 193 nm photon flux, and subsequent electron–ion recombination and radiative decay.

ACKNOWLEDGMENTS

The authors are grateful to the EPSRC for financial support in the form of equipment grants, a Senior Research Fellowship (MNRA) and studentships (F.C. and R.J.L), and to colleagues Dr. P. W. May and Dr. A. J. Orr-Ewing in Bristol, Professor A. Vertes (George Washington University), J. Koivusaari (University of Oulu), and P. A. Cook for their many and varied contributions to this work.

- ¹*Pulsed Laser Deposition of Thin Films*, edited by D. B. Chrisey and G.K. Hubler (Wiley, New York, 1994).
- ²H. M. Smith and A. F. Turner, *Appl. Opt.* **4**, 147 (1965).
- ³A. A. Voevodin and M. S. Donley, *Surf. Coat. Technol.* **82**, 199 (1996).
- ⁴P. Langer, G. Tonon, F. Floux, and A. Ducauze, *IEEE J. Quantum Electron.* **QE-2**, 499 (1966).
- ⁵J. J. Gaumet, A. Wakisaka, Y. Shimizu, and Y. Tamori, *J. Chem. Soc., Faraday Trans.* **89**, 1667 (1993).
- ⁶P. T. Murray and D. T. Peeler, *J. Electron. Mater.* **23**, 855 (1994).
- ⁷S. M. Park and J. Y. Moon, *J. Chem. Phys.* **109**, 8124 (1998).
- ⁸D. B. Geohegan and A. Poretzky, *Mater. Res. Soc. Symp. Proc.* **397**, 55 (1996), and references therein.
- ⁹H. C. Ong and R. P. H. Chang, *Phys. Rev. B* **55**, 13213 (1997).
- ¹⁰F. Kokai and Y. Koga, *Nucl. Instrum. Methods Phys. Res. B* **121**, 387 (1997).
- ¹¹R. J. Lade and M. N. R. Ashfold, *Surf. Coat. Technol.* **120-121**, 313 (1999).
- ¹²D. L. Pappas, K. L. Saenger, J. J. Cuomo, and R. W. Dreyfus, *J. Appl. Phys.* **72**, 3966 (1992).
- ¹³F. Xiong, Y. Y. Yang, V. Leppert, and R. P. H. Chang, *J. Mater. Res.* **8**, 2265 (1993).
- ¹⁴M. Jelinek, V. Olsan, L. Soukup, D. Charalabidis, E. Hontzopoulos, and E. Georgiou, *Diamond Relat. Mater.* **3**, 1128 (1994).
- ¹⁵V. I. Merkulov, D. H. Lowndes, G. E. Jellison, Jr., A. A. Poretzky, and D. B. Geohegan, *Appl. Phys. Lett.* **73**, 2591 (1998).
- ¹⁶C. B. Collins, F. Davanloo, D. R. Jander, T. J. Lee, H. Park, and J. H. You, *J. Appl. Phys.* **69**, 7862 (1991).
- ¹⁷P. J. Fallon, V. S. Veerasamy, C. A. Davis, J. Robertson, G. A. J. Amaratunga, W. I. Milne, and J. Koskinen, *Phys. Rev. B* **48**, 4777 (1993).
- ¹⁸C. B. Collins and F. Davanloo, in Ref. 1, p. 417.
- ¹⁹M. Chhowalla, J. Robertson, C. W. Chen, S. R. P. Silva, C. A. Davis, G. A. J. Amaratunga, and W. I. Milne, *J. Appl. Phys.* **81**, 139 (1997).
- ²⁰Y. Lifschitz, *Diamond Relat. Mater.* **8**, 1659 (1999).
- ²¹K. J. Koivusaari, J. Levoska, and S. Leppävuori, *J. Appl. Phys.* **85**, 2915 (1999).
- ²²R. J. Lade, F. Claeysens, K. N. Rosser, and M. N. R. Ashfold, *Appl. Phys. A: Mater. Sci. Process.* **69**, S935 (1999).
- ²³A. A. Poretzky, D. B. Geohegan, G. E. Jellison, Jr., and M. M. McGibbon, *Appl. Surf. Sci.* **96**, 859 (1996).
- ²⁴A. Neogi, A. Mishra, and R. K. Thareja, *J. Appl. Phys.* **83**, 2831 (1998).
- ²⁵W. L. Wiese, M. W. Smith, and B. M. Miles, *Atomic Transition Probabilities*, Vol. 1, NSRDS-NBS 4, 1966.
- ²⁶A. R. Striganov and N. S. Sventitskii, *Tables of Spectral Lines of Neutral and Ionized Atoms* (IFI/Plenum, New York, 1968).
- ²⁷Y. Yamagata, A. Sharma, J. Narayan, R. M. Mayo, J. W. Newman, and K. Ebihara, *J. Appl. Phys.* **86**, 4154 (1999).
- ²⁸R. Kelly and R. W. Dreyfus, *Surf. Sci.* **198**, 263 (1988).
- ²⁹J. C. S. Kools, T. S. Baller, S. T. De Zwart, and J. Dieleman, *J. Appl. Phys.* **71**, 4547 (1992).
- ³⁰D. B. Geohegan, in Ref. 1, p. 115, and references therein.
- ³¹S. Sasaki, Y. Ohkouchi, S. Takamura, and T. Kato, *J. Phys. Soc. Jpn.* **63**, 2942 (1994).
- ³²H. Schmidt, J. Ihlemann, B. Wolff-Rottke, K. Luther, and J. Troe, *J. Appl. Phys.* **83**, 5458 (1998).
- ³³A. V. Bulgakov and N. M. Bulgakova, *Quantum Electron.* **29**, 433 (1999).
- ³⁴C. R. Phipps and R. W. Dreyfus, in *Laser Ionization Mass Analysis*, edited by A. Vertes, R. Gijbels, and F. Adams (Wiley, New York, 1993), Vol. 124, pp. 369–431, and references therein.